01 Jul 2007

A Three-Dimensional FDTD Subgridding Algorithm with Separated Temporal and Spatial Interfaces and Related Stability Analysis

Kai Xiao

David Pommerenke
Missouri University of Science and Technology, davidjp@mst.edu

James L. Drewniak
Missouri University of Science and Technology, drewniak@mst.edu

A Three-Dimensional FDTD Subgridding Algorithm With Separated Temporal and Spatial Interfaces and Related Stability Analysis

Kai Xiao, *Member, IEEE*, David J. Pommerenke, *Senior Member, IEEE*, and James L. Drewniak, *Fellow, IEEE*

Abstract—A finite-different time-domain subgrid algorithm locally refines the mesh at regions requiring higher resolution. A novel separation of spatial and temporal subgridding interfaces is presented that allows implementing a novel spatial subgridding method and investigating the stability of each subalgorithm individually. Details are given for a spatial subgridding algorithm having a 1:3 mesh ratio. In the spatial subgridding algorithm, the fine-mesh is constructed with a recessed interface and the interpolation scheme is designed to be symmetric to maintain the stability of the update process. The stability of the spatial subgridding algorithm is analyzed with a matrix method. Numerical examples showing stability and accuracy are provided.

Index Terms—Finite-difference time-domain (FDTD), stability, subgrid.

I. INTRODUCTION

SINCE its introduction by K. S. Yee in 1966 [1], the finite-difference time-domain (FDTD) method has been widely used due to its simplicity and ability to handle complicated geometries and inhomogeneous media. The conventional explicit Yee scheme is only conditionally stable, and the maximum stable time increment is limited by the smallest cell. Long computational times are required if a uniform Cartesian mesh is used in a mixed-scale problem as the time step is determined by the smallest cell needed to model the geometry.

In a subgridding algorithm, the fields in the grid at the interface need to be estimated through some interpolation scheme, which may introduce late-time instability. In addition, the numerical reflections at the subgridding interface and the different numerical dispersions in the two meshes will compromise the modeling accuracy. The essential issue of a subgridding algorithm is to develop a field coupling scheme that should not introduce instability, and at the same time provide results of known accuracy.

Handling the subgridding interface has been the topic of many papers [3]–[14]. In an early paper, a two-step update scheme is used [3], in which fields obtained from the update in the

coarse mesh will serve as the boundary conditions for the following update in the fine meshes after interpolated in time and space. In [4], the variable step size method (VSSM) proposed two schemes that can simultaneously update the fields in the coarse and fine meshes, the direct interpolation for a 2:1 mesh ratio and the wave equation based interpolation for a 3:1 ratio. The wave equation based schemed was later improved in the mesh refinement algorithm (MRA) [5] and the multigrid displacement method (MGDM) [6]. In MGDM, an intuitive "soft" transition approach is introduced in which three overlapping layers are used to make a smooth transition between coarse and fine meshes to improve the stability.

In [7], a subgridding algorithm allowing material across subgridding interface for odd mesh ratios is proposed based on the direct interpolation in space and time. To mitigate the numerical reflection at the interface, higher order interpolation and spline functions are used in [8], and an innovative "pulsing overlapping" mesh is used, in which the outer layer of the fine mesh is dropped subsequently in the cycles of the field update, and the fine mesh is restored to the original size at the end of the cycle. The multigrid current method (MGCM) proposed in [9] which can also handle material traverse, uses an area-weight scheme to interpolate the electric current based on Ampere's law instead of the direct interpolation of fields.

Late-time instability is always an issue for a subgridding algorithm. In general, two remedial methods were used to address the instability issue: 1) smoothing the field transition by averaging the fields at the subgridding interface with the neighboring field values [6], [7], [9]; and, 2) applying an empirical reduction factor to the Courant limit to reduce the time increment [6]–[9]. However, no analytical analysis has been published with respect to the success of these remedies.

In [10], and later improved and reported in [11] and [12], a consistent subgridding algorithm was developed in the framework of the finite integration technique (FIT). The stability of this method is ensured by maintaining the consistency of field coupling scheme. A mesh ratio of two is adopted and a weighted area interpolation scheme is applied to preserve both the electric and magnetic flux conservation. Another scheme also considering the consistency of field coupling scheme is provided in [13], which is based on an equivalent passive network method.

The subgridding method presented in this paper is novel in two aspects. First, the domain interfaces for space and time refinement are separated. This allows the implementation of a novel spatial field interpolation algorithm, which maintains the symmetry of Yee's algorithm and ensures stability. In the
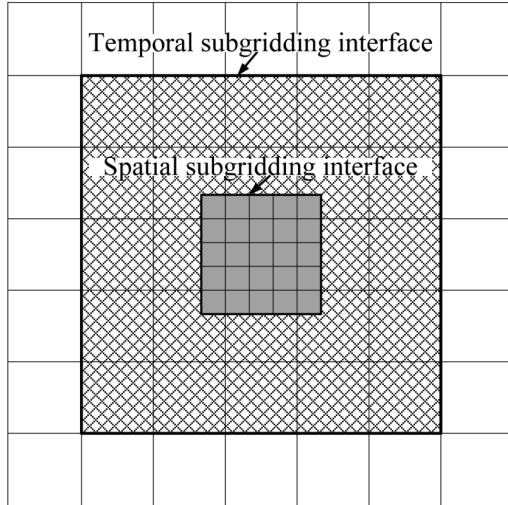
Fig. 1.   Separate FDTD spatial and temporal subgridding interfaces.

present implementation, the algorithm does not allow material to across the spatial subgridding interface. Both mesh ratios two and three have been implemented. The stability of the algorithm is outlined by the iterative formulation.

The rest of this paper is organized as follows. The overview of separating spatial and temporal subgridding interfaces is given in Section II. In Sections III and IV, the spatial and temporal subgridding algorithms are described in detail. Section V gives the numerical examples, and conclusions are drawn in Section VI.

II. Separating Spatial and Temporal Subgridding Interface

It is more efficient to have the time increment adaptive to local meshes in the subgridding algorithm. Most of the subgridding methods of this type merge the spatial and temporal subgridding to a unified algorithm, and there is only one interface for both subgridding processes.

The spatial and temporal subgridding interfaces, however, are not necessarily coincident with each other, as shown in Fig. 1. We introduce the separated interfaces, allowing the spatial subgridding and temporal algorithm to be implemented separately. The stability and accuracy can also be tested and analyzed individually.

The implementation of the combined algorithm is shown in Fig. 1. The location of the temporal and spatial subgridding interfaces are first selected with at least one grid cell between them, and the temporal and spatial subgridding algorithms are applied on the related interfaces, respectively.

III. FDTD Spatial Subgridding Algorithm

It has been pointed out in [10] that stability can be ensured only if the consistency in the field coupling scheme at subgridding interface is maintained, e.g., if an e-field is involved in updating an e-field, this e-field will be used in the update of the e-field in the following time step. The interpolation coefficients used in the spatial subgridding should not break the symmetry in the original Yee update scheme.

A. Symmetry of Yee's Update Scheme

The standard FDTD update equations in matrix form in a source-free and lossless region can be written as

$$\begin{cases} \mathbf{H}^{n+\frac{1}{2}} = \mathbf{H}^{n-\frac{1}{2}} - \Delta t \mathbf{M}_\mu^{-1} \mathbf{S}_h^{-1} \mathbf{D}_e \mathbf{l}_e \mathbf{E}^n \\ \mathbf{E}^{n+1} = \mathbf{E}^n + \Delta t \mathbf{M}_\varepsilon^{-1} \mathbf{S}_e^{-1} \mathbf{D}_h \mathbf{l}_h \mathbf{H}^{n+\frac{1}{2}} \end{cases} \quad (1)$$

where $\mathbf{E}$ and $\mathbf{H}$ are the update variables in one dimensional vectors; $\mathbf{M}_\varepsilon$ and $\mathbf{M}_\mu$ are diagonal matrices that represent the material properties; $\mathbf{l}_e$ and $\mathbf{l}_h$ are diagonal matrices that define the length of the cell edges of the related field components; $\mathbf{S}_e$ and $\mathbf{S}_h$ are also diagonal matrices, defining the surface areas perpendicular to the related field components; and, $\mathbf{D}_e$ and $\mathbf{D}_h$ are two very sparse matrices that define the curl operators in matrix form, consisting of non-zero entries of either $+1$ or -1. It can be shown that the two matrices are symmetric [10], [15],

$$\mathbf{D}_h = \mathbf{D}_e^T. \quad (2)$$

Consider the update of the e-field from time step $(n-1)$ to $(n+1)$. By eliminating h-field terms, an iterative formulation of the e-field can be obtained

$$\mathbf{E}^{n+1} - \left(2\mathbf{I} - \Delta t^2 \mathbf{M}_\varepsilon^{-1} \mathbf{S}_e^{-1} \mathbf{D}_h \mathbf{l}_h \mathbf{M}_\mu^{-1} \mathbf{S}_h^{-1} \mathbf{D}_e \mathbf{l}_e \right) \mathbf{E}^n \\ + \mathbf{E}^{n-1} = 0. \quad (3)$$

Equation (3) can also be obtained by directly discretizing the wave equation. Define $\mathbf{A} = \mathbf{M}_\varepsilon^{-1} \mathbf{S}_e^{-1} \mathbf{D}_h \mathbf{l}_h \mathbf{M}_\mu^{-1} \mathbf{S}_h^{-1} \mathbf{D}_e \mathbf{l}_e$. It can be shown that $\mathbf{A}$ is a positive semi-definite symmetric matrix. If the time increment satisfies the Courant criteria, the update process is stable [14]–[16]. To keep the FDTD update process stable, the field interpolation introduced by the subgridding algorithm should not break the symmetry and positive semi-definite properties of matrix $\mathbf{A}$. However, the preservation of symmetry of the interpolation scheme in a practical subgridding algorithm is not trivial.

B. Two-Dimensional Spatial Subgridding Algorithm

In a subgridding algorithm, the construction of the fine mesh, the selection of the mesh ratio, and the design of the interpolation scheme are closely related. In the proposed spatial subgridding, the fine mesh is constructed to be recessed from the coarse grid surface, as shown in Fig. 2 for a two-dimensional mesh with a 1:3 mesh ratio. In Fig. 2, the upper case "E" and "H" denote the coarse-cell fields at the subgridding interface, and the lower case "e" and "h" denote the fine-cell fields. The locations of coarse-cell h-fields are marked with a circle "○," the fine-cell h-fields a dot "●," and the collocated h-fields are marked with a circle with a dot inside "⊙." Compared to the subgrid in [8], the subgrid in Fig. 2 has no cells overlapping both the coarse and fine meshes. In addition, the recessed fine mesh introduces cells with reduced size and non-rectangular shape at the interface. The arrangement in Fig. 2 is intended to facilitate a symmetric interpolation pattern.

The field-coupling scheme from coarse-mesh to fine-mesh (forward coupling), and the scheme from fine-mesh to coarse-mesh (backward coupling) are illustrated in Fig. 3. In Fig. 3(a), the "missing" fine-cell h-fields are interpolated from the known coarse-cell h-fields. With the interpolated h-field values, the
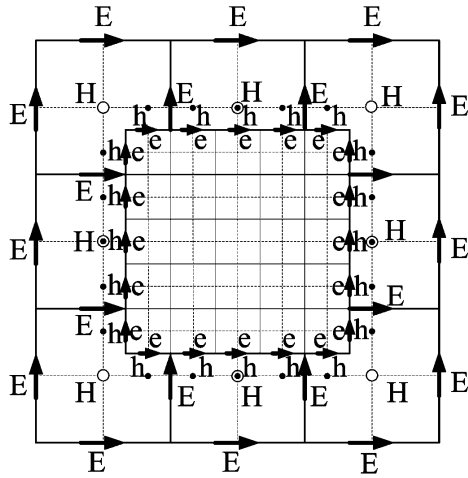
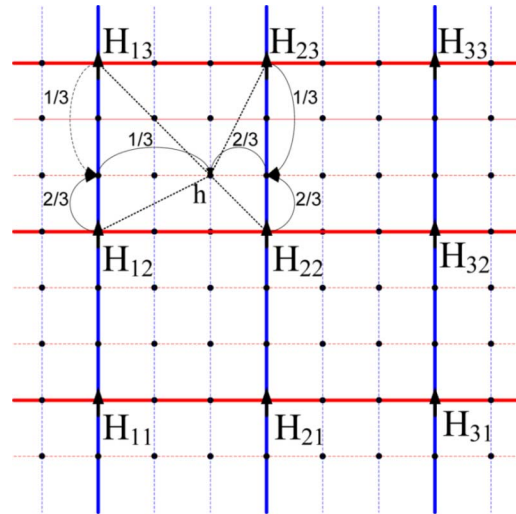Fig. 2. The construction of a fine mesh of ratio three in 2D.
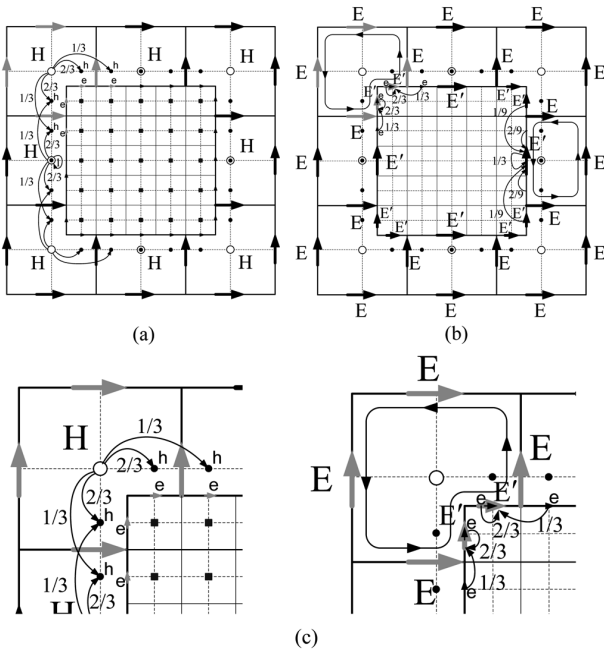

(a)   (b)

(c)

Fig. 3. (a) Forward and (b) backward field coupling schemes for the FDTD spatial subgridding algorithm; (c) zoomed view of the corner cell.

Fig. 4. 2-D linear interpolation at a 3-D subgridding interface.

components contribute to the loop integral of the magnetic current, although some e-fields in the fine mesh are not physically located on the integral path. The e-fields indicated with E' in Fig. 3(c) are actually interpolated from the e-fields, "e," in the fine mesh on the subgridding interface. It should be noted that the corner cells in the coarse mesh are no longer rectangular if the recessed mesh is used. The field update, however, can be continued by calculating the current densities [19].

C. Three-Dimensional Spatial Subgridding Algorithm

The interpolation scheme needs to be extended to the additional axis directions when applied to three dimensions. Fig. 4 shows the two-dimensional linear interpolation scheme on a 3-D subgridding interface [11]. For example, the fine-cell h-field "h" can be interpolated by the four neighboring coarse-cell h-fields

$$h = \frac{1}{3}\left(\frac{1}{3}H_{13} + \frac{2}{3}H_{12}\right) + \frac{2}{3}\left(\frac{1}{3}H_{23} + \frac{2}{3}H_{22}\right)$$
$$= \frac{1}{9}H_{13} + \frac{2}{9}H_{12} + \frac{2}{9}H_{23} + \frac{4}{9}H_{22}. \tag{4}$$

The interpolation scheme can be extended to the other mesh ratios.

The construction of a three-dimensional fine-mesh is illustrated in Fig. 5 for an h-field at the coarse mesh along the subgridding interface but not at the edge. The fine-cell h-fields at the interface are interpolated from the neighboring coarse-cell h-fields. In general, a coarse-cell h-field is involved in the interpolation of 25 fine-mesh h-fields, and thereafter the update of 25 fine-cell e-fields. In the following time-step, the same number of fine-mesh e-fields at the subgridding interface will be involved in the update of the related coarse-mesh h-field through the backward interpolation scheme. For example, in Fig. 5, the h-field at the interface in the coarse mesh, $\tilde{H}_z^{i,j,k}$, is interpolated to 25 h-fields in the fine mesh, as indicated with z-axis oriented arrows and the related interpolation coefficients. Once these h-fields are known, the e-fields at the subgridding interface, $\tilde{e}_x^{o+i,p,q+j}$, $i,j = 0, \pm 1 \pm 2$, then can be updated. Therefore, the H-field in the coarse mesh, $\tilde{H}_z^{i,j,k}$, is indirectly involved in the update of the 25 e-fields in the fine mesh,

e-field update in can be completed in the fine-mesh. In the next time step, the "missing" coarse cell e-fields can be interpolated from the known e-field in the fine mesh, and the h-field update in the coarse-mesh can be continued. Comparing the interpolation patterns as indicated by the coefficients associated with the arrows in Fig. (3a) and (b), it can be seen that forward and backward coupling schemes are symmetric. For example, as shown in Fig. 3(c), in the forward coupling scheme, the h-field in the upper left corner, as indicated by "H," is used to interpolate the four h-fields in the fine mesh at the interface, as indicated with "h." With these four interpolated h-fields, the e-fields in fine mesh, as indicated with "e," at the interface can be updated. Thus, the h-field, "H," is involved in the update of four e-field components in the coarse mesh and four in the fine-mesh indirectly through interpolation, as marked with grey arrows. In the backward coupling scheme, all these e-field
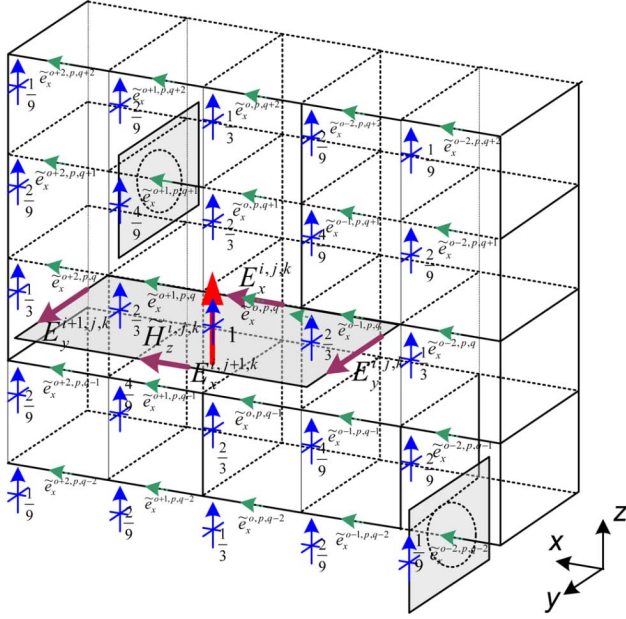
Fig. 5. The interpolation pattern for an H-field in coarse mesh in three dimensions.

$\tilde{e}_x^{o+i,p,q+j}$, $i,j = 0,\pm1\pm2$, through interpolation. In the next time step, e-field $E_x^{i,j,k}$ is calculated by interpolating these e-fields, $\hat{e}_x^{o+i,p,q+j}$, $i,j = 0,\pm1\pm2$. Then, $E_x^{i,j,k}$ along with $E_y^{i+1,j,k}$, $E_x^{i,j+1,k}$, and $E_y^{i,j,k}$ are used to update $\hat{H}_z^{i,j,k}$. Therefore, the 25 e-fields, $\tilde{e}_x^{o+i,p,q+j}$, $i,j = 0,\pm1\pm2$, are also indirectly involved in the calculation of $E_x^{i,j,k}$.

If the coefficients of the forward and backward interpolation pattern are selected accordingly, the subgridding schemes will be consistent to ensure the stability.

It is important to note that the interpolation pattern needs to be changed at the edges of the subgridding interface, as shown in Fig. 6. Fig. 6(a) gives the combined coarse and fine meshes at the termination edge, and Fig. 6(b) shows only the fine mesh with interpolation pattern. The h-field at the bottom of the fine mesh, which is indicated with underlined interpolation coefficients in Fig. 6(b), normally should be interpolated by the neighboring four h-field components in the coarse mesh, H_{z1}, H_{z2}, H_{z3}, and H_{z4}, as indicated with bold letters. The loop integral of the e-field components in the coarse mesh for H_{z3} and H_{z4}, however, is complete. If H_{z3} and H_{z4} are used in the interpolation, it is difficult to maintain the symmetry of the interpolation scheme, and late-time instability may occur. Therefore, special treatment should be applied, as shown in Fig. 6(b), and, H_{z3} and H_{z4} will not be used in the interpolation. Such changes will introduce numerical errors in the corner cells. However, this is a compromise between accuracy and stability. To improve the accuracy of the subgridding algorithm, higher order interpolation schemes can be used, but the symmetry of the forward and backward coupling schemes should be maintained. Optimal interpolation schemes were discussed in [17] for a two-dimensional situation. In a recent paper [18], the idea of the digital filtering, numerical wave impedance matching, and domain overriding is introduced to reduce the spurious reflections at the subgridding interface, and the two-dimensional results show these approaches are very promising to extend to three dimensions.
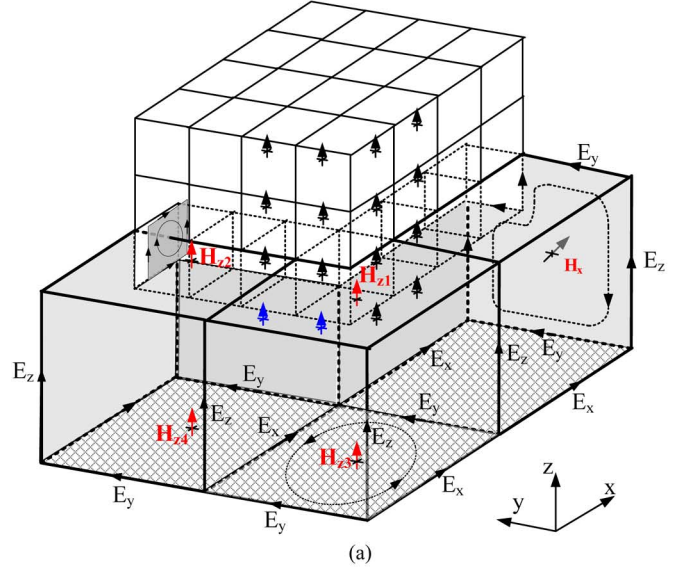

(a)

(b)

Fig. 6. The interpolation pattern at the termination edge. (a) Combined the coarse and fine meshes at the termination edge. (b) fine-mesh at the termination edge.

D. Update Procedure of the Spatial Subgridding Algorithm

The summary of the update process is given Fig. 7, where $\mathbf{E}, \mathbf{H}, \mathbf{e}$, and $\mathbf{h}$ are the field components in the coarse mesh and fine mesh, that are not involved in the interpolation, respectively; while the fine-cell h-fields ($\tilde{\mathbf{h}}$) are interpolated from the coarse-cell h-fields ($\hat{\mathbf{H}}$); while the coarse-cell e-fields at the interface ($\tilde{\mathbf{E}}$) are obtained from the fine-cell e-fields ($\tilde{\mathbf{e}}$). All the $\mathbf{D}$ matrices with subscript or superscript are the sub-blocks of the curl operator matrix, and the $\mathbf{P}$ and $\mathbf{Q}$ are the interpolation matrices.

Suppose that the field update has been advanced to time step n, and all the h-fields in the coarse mesh and fine mesh are known. The update process from time step n to $(n + 1)$ is implemented as follows.

1. Time step $= (n + 1/2)$.
   a. Update e-fields ($\mathbf{E}$) in the coarse mesh based on h-fields inside the mesh ($\mathbf{H}$) and those at the subgridding interface ($\hat{\mathbf{H}}$), shown as step 1 in Fig. 7.
   b. Update e-fields in the fine mesh (inside fine mesh "e" and at the interface $\tilde{\mathbf{e}}$), based on the h-fields inside the fine mesh ($\mathbf{h}$) and at the interface ($\tilde{\mathbf{h}}$), shown as steps 2 and 3 in Fig. 7.
   c. Calculate the e-fields ($\tilde{\mathbf{E}}$) on the subgridding interface in the coarse mesh by interpolating the e-fields ($\tilde{\mathbf{e}}$)
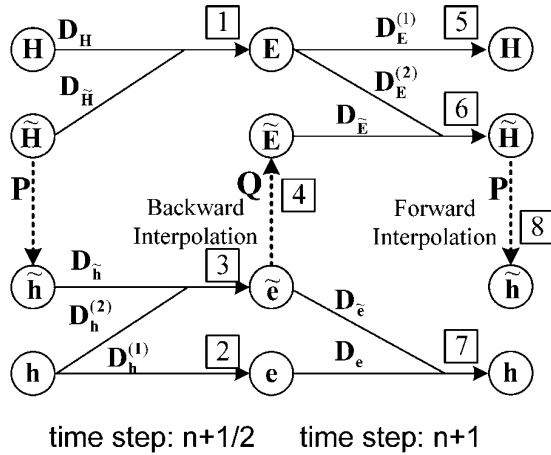
Fig. 7. Flow chart of the subgridded FDTD update scheme.

at the interface in the fine mesh. The interpolation pattern is defined by matrix $\mathbf{Q}$, shown as step 4 in Fig. 7.
  d. Enforce the boundary conditions in the coarse mesh.
  e. Advance simulation time: $t = t + dt/2$.
  2. Time step $= (n + 1)$.
  a. Update the h-fields in the coarse mesh both inside mesh "$\mathbf{H}$" and on the subgridding interface "$\tilde{\mathbf{H}}$" based on the e-fields inside the coarse mesh ($\mathbf{E}$) and at the interface ($\tilde{\mathbf{E}}$), shown as step 5 and 6.
  b. Update the h-fields in the fine mesh ($\mathbf{h}$) based on the e-fields inside the fine mesh ($\mathbf{e}$) and at the interface ($\tilde{\mathbf{e}}$), shown as step 7.
  c. Calculate the h-field in the fine mesh at the interface ($\tilde{\mathbf{h}}$) by interpolating the h-field ($\tilde{\mathbf{H}}$) at the interface in the coarse mesh. The interpolation pattern is defined by matrix $\mathbf{P}$, shown as step 8.
  d. Advance simulation time: $t = t + dt/2$.
  3. Repeat 1 and 2 until the simulation stops.
  A detailed stability analysis is outlined in the Appendix.

Although only a spatial subgridding with a refinement ratio of three is shown here, a refinement ratio of two was also implemented [19]. Higher mesh ratios can be achieved by either directly extending the interpolation scheme to higher ratios or cascading the ratios of 1:2 and 1:3.

IV. TEMPORAL SUBGRIDDING ALGORITHM

A subgridding algorithm is more efficient if time increment is adaptively selected in the different meshes. Ideally, the temporal interface should be collocated with the spatial interface for the maximum efficiency. However, since cells with reduced size or even non-rectangular shape are introduced at the subgridding interface, it is necessary to separate the temporal and spatial interfaces.

Linear or higher order interpolation and extrapolation are commonly used in the temporal subgridding scheme [5]–[9]. Higher-order schemes will yield smoother time-domain waveforms. However, it is found that late-time instability often occurs for the schemes using extrapolation. The scheme given
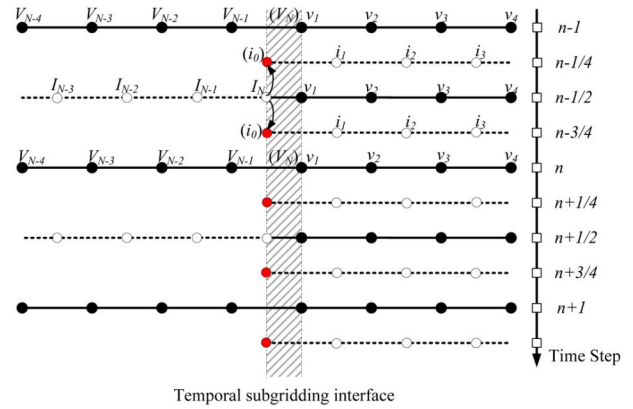

Fig. 8. Time-space diagram of a temporal subgridding scheme.

in [10] that assumes the field components at the subgridding interface remain constant in the sub-cycles of one coarse time step was reported to be stable through numerical examples. The same scheme is also used in this paper. The space-time diagram for a temporal subgridding with a ratio of two for a one-dimensional update scheme is shown Fig. 8. The shadowed region is the temporal subgridding interface, where the fields at the time steps need to be estimated from the known field values at the coarse time-steps. The advantage of this scheme is that no extrapolation in time is used. A similar idea is also addressed in [2].

V. NUMERICAL EXAMPLES

The spatial and temporal subgridding algorithms were implemented, and the stability and accuracy of these algorithms was tested numerically.

A. Stability

To test the stability of the spatial subgridding algorithm, a model of a cavity is simulated, as shown in Fig. 9. The model consists of a dipole antenna, which is implemented with two PEC arms connected with a lumped 50 Ω voltage source. Each arm of the dipole is 7-cell long, and the cross-section is 2 cells by
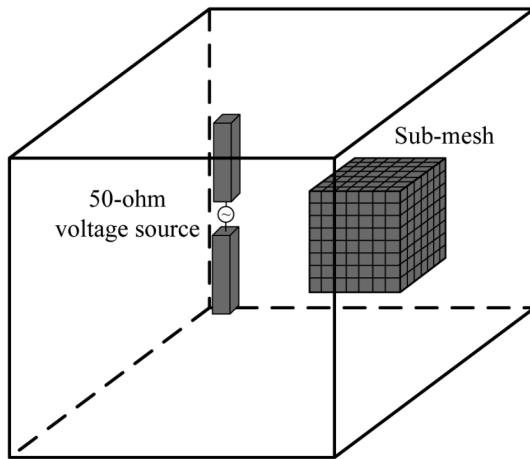
Fig. 9.   Numerical model for stability test of the spatial subgridding algorithm.
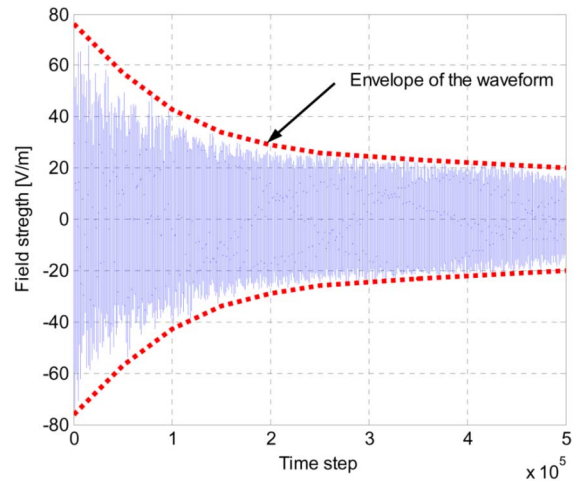

Fig. 10.   The excitation Gaussian pulse with unit amplitude.

Fig. 11.   The e-field waveform at the center of the fine mesh.

Fig. 12.   Two-dimensional cross-section of the second stability test model.

2 cells. The excitation is a Gaussian pulse, as shown in Fig. 10. The cross-section of the dipole is meshed by four cells, and the two arms are centered at (10, 20, 20) with a cell in between. PEC boundary conditions are used. A subgridded domain is set in the vacuum. The computational domain is $40 \times 40 \times 40$ cells if filled with coarse cells, and the dimensions for one cell are 5 cm by 5 cm by 5 cm. The two diagonal points of the spatial subgrid are located at (16, 11, 11) and (35, 29, 29) in terms of the coarse cell, and the refinement ratio is three. The only loss mechanism for energy coupled into this resonator is the 50 Ω source impedance of the dipole.

Fig. 11 shows the time-domain e-field values at the center of the subgrid. After half a million time steps, no sign of instability is observed. The envelope of the e-field waveform indicates that the update process is stable, and the energy is gradually attenuated.

A model of a lossless dielectric sphere with a dielectric constant of four in a resonance cavity was used to test the stability of the combined temporal subgridding method. The source is an incident plane wave from $-z$ direction, implemented with the scattered field met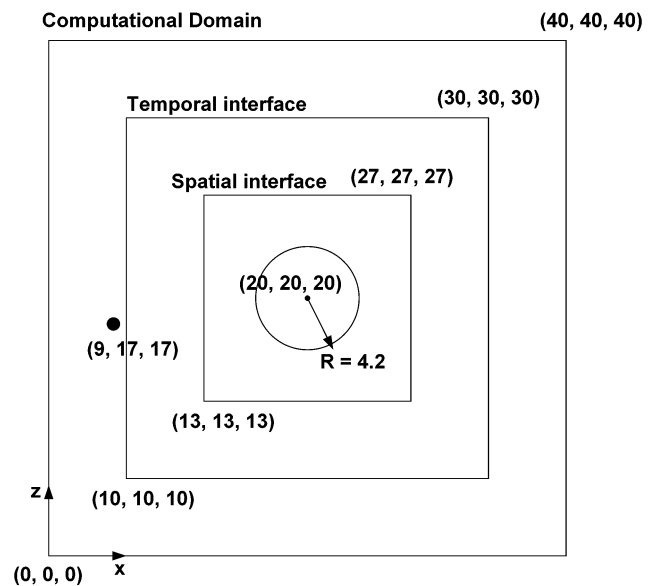hod. Fig. 12 gives the two-dimensional cross-section of the model. The boundary conditions are set to be PEC, and the same excitation waveform was used with an amplitude of 1000 V/m. The refinement ratios for temporal and spatial subgridding scheme were both three. A field probe was put right before the temporal subgridding interface in the main-grid. The waveform of the x-component of the E-field at the probe is shown in Fig. 13. After half a million steps (one and a half million steps in the subgrid), no sign of instability is observed.

Coordinates (x,y,z) in Fig. 12 refer to the grid index in the homogeneous mesh.

The fact that both the spatial and temporal subgridding algorithms are stable will favor the stability of the combined scheme, which is supported by the numerical result in Fig. 13. The stability of the individual algorithm, however, does not naturally lead to the stability of the combined algorithm. A complete proof for the stability of the combined scheme is difficult and is a topic that the authors are working on.
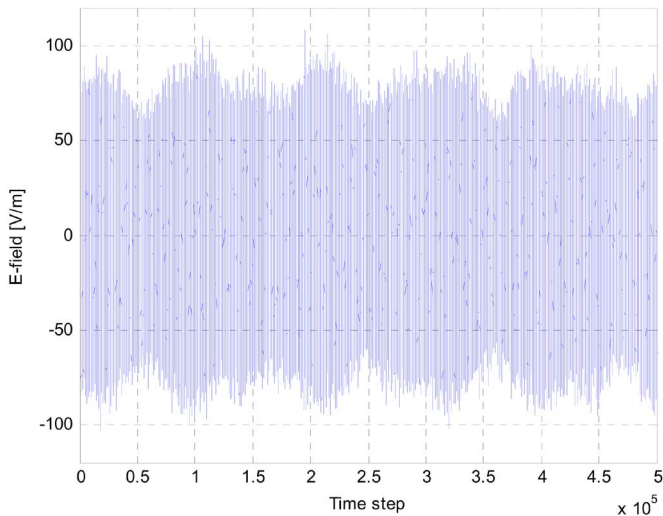
Fig. 13. The Ex waveform of the combined spatial and temporal subgridding model ($\Delta t = 9.63$e-11ps in main-grid).
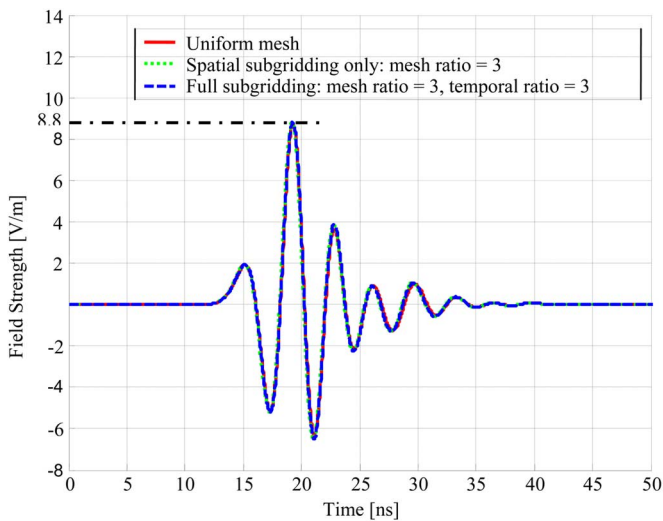

Fig. 14. The E-field wave in the front of the fine mesh.

B. Accuracy

To examine the accuracy of the algorithms, a model similar to that shown in Fig. 9, is calculated. The size of the computational domain is 100 by 30 by 30 cells. Two arms of the dipole antenna are centered at (10, 10, 15), and separated by one cell. Each arm is 7-cell long, and has a cross-section of $7 * 7$ cells. The excitation waveform was a Gaussian pulse, the same as that in the first example as given in Fig. 10. Second order Mur absorbing boundary conditions were used. The coordinates of the two diagonal corners of the spatial subgrid normalized to the cell length are (80, 10, 10) and (90, 20, 20). The temporal subgridding interface is one cell away from the spatial interface. A probe is placed directly in the front of the mesh at (76, 15, 15). The e-field waveforms with and without the subgrid are compared in Fig. 14. The difference between the waveforms of the subgridded mesh and the uniform mesh is defined as the numerical reflection from the mesh, as shown in Fig. 15. As can be seen in Fig. 15, the reflection of the full subgridding algorithm is only slightly greater than that of the spatial algorithm. For
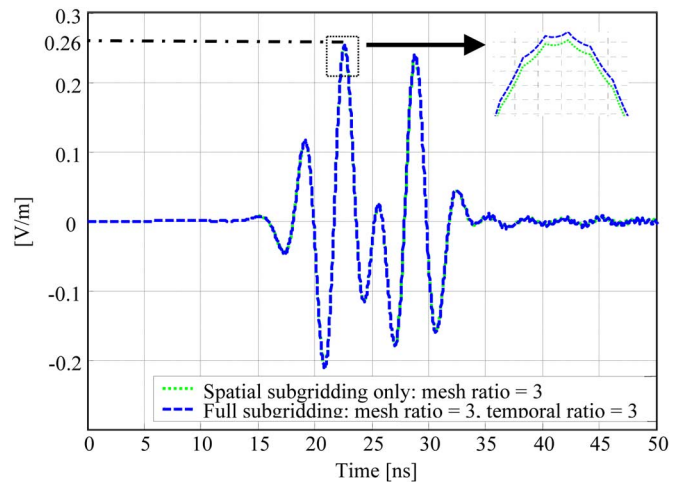

Fig. 15. The time-domain reflection of the subgridding algorithm.

example, the peak value of the field waveform is 8.8 V/m, and the peak value of the numerical reflection curve is about 0.26 V/m, as shown in Figs. 14 and 15. The test model here gives the accuracy only from one perspective. Actually, stability and accuracy of a subgridding algorithm are closely related two issues. Stability can be ensured by maintaining the reciprocity, and the accuracy can be improved by applying a more precise interpolation scheme.

As discussed at the beginning of the paper, the main purpose of a subgridding algorithm is to improve the modeling efficiency. Table I gives the run time comparison for the example in the accuracy test. The only difference in the last case is that five layers of cells are placed between the spatial and temporal subgridding interfaces in order to better quantify the impact of separation of the interface separation upon computation time.

Table I shows that the ratio of run times between the uniform fine mesh and spatial-only subgridded mesh is roughly equal to the ratio of the total number of cells. Another observation from Table I is that several layers of cells between the spatial and temporal interfaces only have a limited impact on the overall modeling efficiency, since the run time ratio between the last two cases in Table I is very close to three.

VI. CONCLUSION

A combined spatial and temporal subgridding algorithm is proposed in this paper. The two novel aspects of this scheme are the separation of temporal and spatial subgridding interfaces, and the spatial mesh construction and field coupling scheme.

The separation of subgridding interfaces simplifies the development and analysis of the spatial and temporal algorithms, and provides additional flexibility in applying the subgridding scheme. The spatial subgridding algorithm is described in detail for both 2-D and 3-D implementations. The fine-mesh is constructed with a recessed subgridding interface, which makes it possible to design a symmetric and consistent field interpolation scheme. Two different mesh ratios (two and three) were implemented and the stability of the spatial scheme was analyzed using the matrix method. In the present implementation, no material is allowed to traverse the subgridding interface, and the authors are working in this direction in the subsequent research.

TABLE I
RUN TIME COMPARISON OF THE SUBGRIDDING ALGORITHM

Simulation Case (refinement ratio = 3)	number of cells in base-grid	number of cells in spatial sub-grid	number of cells in temporal sub-grid *	computational time (s)
uniform fine mesh	2,430,000	n/a	n/a	6453
spatial only subgridding	90,000	19683	n/a	286
combined spatial and temporal subgridding	90,000	19683	7000	97

Note (*): the spatially subgridded cells have been excluded from the total number of cells in the temporal sub-grid to avoid double counting

The stability of the spatial and temporal subgridding algorithms was tested numerically. For the range of the examined examples, the obtained results showed the stability of the algorithm. The accuracy of the algorithms was also tested by measuring the time-domain reflection at the subgridding interface.

APPENDIX

Based on the flow chart in Fig. 7, the field update equations with a subgrid can be written as in (A1), shown at the bottom of the page, where $\mathbf{I}$ denotes a unit matrix, $\mathbf{S}$ is a diagonal matrix defining the area of the surface that the discrete curl operation applies, and the descriptions of other variables can be found in the legend of Fig. 7. Furthermore, define $\tilde{\mathbf{E}} = \mathbf{Q}\tilde{\mathbf{e}}$ and $\tilde{\mathbf{h}} = \mathbf{P}\tilde{\mathbf{H}}$, where $\mathbf{P}$ and $\mathbf{Q}$ are the interpolation matrices. Assume that the mesh is homogeneous. For the subgridding scheme with a ratio of three, the edge length ratio of a fine cell to a coarse cell is 1/3. After normalizing all the edge lengths to that of a coarse cell, (A1) can be rewritten as (A2), shown at the bottom of the page, where l is the edge length of a coarse cell.

Then, define

$$\bar{\mathbf{D}}_{\mathbf{E}} = \begin{pmatrix} \mathbf{D}_{\mathbf{E}}^{(1)} & 0 & 0 \\ \mathbf{D}_{\mathbf{E}}^{(2)} & \mathbf{D}_{\tilde{\mathbf{E}}}\mathbf{Q} & 0 \\ 0 & \frac{1}{3}\mathbf{D}_{\tilde{\mathbf{e}}} & \frac{1}{3}\mathbf{D}_{\mathbf{e}} \end{pmatrix}$$

and

$$\bar{\mathbf{D}}_{\mathbf{H}} = \begin{pmatrix} \mathbf{D}_{\mathbf{H}} & \mathbf{D}_{\tilde{\mathbf{H}}} & 0 \\ 0 & \frac{1}{3}\mathbf{D}_{\tilde{\mathbf{h}}}\mathbf{P} & \frac{1}{3}\mathbf{D}_{\mathbf{h}}^{(2)} \\ 0 & 0 & \frac{1}{3}\mathbf{D}_{\mathbf{h}}^{(1)} \end{pmatrix}.$$

The curl operator matrices for the h-field and e-field in either the coarse mesh or fine mesh are mutual transpose matrices if the cells on the subgridding interface are not considered, which means that

$$\begin{cases} \begin{pmatrix} \mathbf{D}_{\mathbf{E}}^{(1)} \\ \mathbf{D}_{\mathbf{E}}^{(2)} \end{pmatrix} = \begin{pmatrix} \mathbf{D}_{\mathbf{H}} & \mathbf{D}_{\tilde{\mathbf{H}}} \end{pmatrix}^{T} \\ \begin{pmatrix} \mathbf{D}_{\mathbf{h}}^{(2)} \\ \mathbf{D}_{\mathbf{h}}^{(1)} \end{pmatrix} = \begin{pmatrix} \mathbf{D}_{\tilde{\mathbf{e}}} & \mathbf{D}_{\mathbf{e}} \end{pmatrix}^{T} \end{cases}. \tag{A3}$$

It should be noted, however, that the symmetry of the interpolation scheme does not imply that $\mathbf{Q} = \mathbf{P}^{T}$. This is because $\tilde{\mathbf{E}} = \mathbf{Q}\tilde{\mathbf{e}}$ and $\tilde{\mathbf{h}} = \mathbf{P}\tilde{\mathbf{H}}$, and the dimensions of the vectors $\tilde{\mathbf{E}}$ and $\tilde{\mathbf{H}}$ are not necessarily the same. Based on the subgridding scheme illustrated in Fig. 7, the relation between the forward and backward interpolation matrices is

$$\mathbf{D}_{\tilde{\mathbf{h}}}\mathbf{P} = \frac{1}{9}(\mathbf{D}_{\tilde{\mathbf{E}}}\mathbf{Q})^{T}. \tag{A4}$$

$$\begin{cases} \begin{pmatrix} \mathbf{H} \\ \tilde{\mathbf{H}} \\ \mathbf{h} \end{pmatrix}_{n+\frac{1}{2}} = \begin{pmatrix} \mathbf{H} \\ \tilde{\mathbf{H}} \\ \mathbf{h} \end{pmatrix}_{n-\frac{1}{2}} - \Delta t\mu^{-1}\begin{pmatrix} \mathbf{S}_{\mathbf{H}} & 0 & 0 \\ 0 & \mathbf{S}_{\tilde{\mathbf{H}}} & 0 \\ 0 & 0 & \mathbf{S}_{\mathbf{h}} \end{pmatrix}^{-1}\begin{pmatrix} \mathbf{D}_{\mathbf{E}}^{(1)} & 0 & 0 & 0 \\ \mathbf{D}_{\mathbf{E}}^{(2)} & \mathbf{D}_{\tilde{\mathbf{E}}} & 0 & 0 \\ 0 & 0 & \mathbf{D}_{\tilde{\mathbf{e}}} & \mathbf{D}_{\mathbf{e}} \end{pmatrix}\begin{pmatrix} \mathbf{l}_{\mathbf{E}} & 0 & 0 & 0 \\ 0 & \mathbf{l}_{\tilde{\mathbf{E}}} & 0 & 0 \\ 0 & 0 & \mathbf{l}_{\tilde{\mathbf{e}}} & 0 \\ 0 & 0 & 0 & \mathbf{l}_{\mathbf{e}} \end{pmatrix}\begin{pmatrix} \mathbf{I}_{\mathbf{E}} & 0 & 0 \\ 0 & \mathbf{Q} & 0 \\ 0 & \mathbf{I}_{\tilde{\mathbf{e}}} & 0 \\ 0 & 0 & \mathbf{I}_{\mathbf{e}} \end{pmatrix}\begin{pmatrix} \mathbf{E} \\ \tilde{\mathbf{e}} \\ \mathbf{e} \end{pmatrix}_{n} \\ \begin{pmatrix} \mathbf{E} \\ \tilde{\mathbf{e}} \\ \mathbf{e} \end{pmatrix}_{n+1} = \begin{pmatrix} \mathbf{E} \\ \tilde{\mathbf{e}} \\ \mathbf{e} \end{pmatrix}_{n} + \Delta t\varepsilon^{-1}\begin{pmatrix} \mathbf{S}_{\mathbf{E}} & 0 & 0 \\ 0 & \mathbf{S}_{\tilde{\mathbf{e}}} & 0 \\ 0 & 0 & \mathbf{S}_{\mathbf{e}} \end{pmatrix}^{-1}\begin{pmatrix} \mathbf{D}_{\mathbf{H}} & \mathbf{D}_{\tilde{\mathbf{H}}} & 0 & 0 \\ 0 & 0 & \mathbf{D}_{\tilde{\mathbf{h}}} & \mathbf{D}_{\mathbf{h}}^{(2)} \\ 0 & 0 & 0 & \mathbf{D}_{\mathbf{h}}^{(1)} \end{pmatrix}\begin{pmatrix} \mathbf{l}_{\mathbf{H}} & 0 & 0 & 0 \\ 0 & \mathbf{l}_{\tilde{\mathbf{H}}} & 0 & 0 \\ 0 & 0 & \mathbf{l}_{\tilde{\mathbf{h}}} & 0 \\ 0 & 0 & 0 & \mathbf{l}_{\mathbf{h}} \end{pmatrix}\begin{pmatrix} \mathbf{I}_{\mathbf{H}} & 0 & 0 \\ 0 & \mathbf{I}_{\tilde{\mathbf{H}}} & 0 \\ 0 & \mathbf{P} & 0 \\ 0 & 0 & \mathbf{I}_{\mathbf{h}} \end{pmatrix}\begin{pmatrix} \mathbf{H} \\ \tilde{\mathbf{H}} \\ \mathbf{h} \end{pmatrix}_{n+\frac{1}{2}} \end{cases} \tag{A1}$$

$$\begin{cases} \begin{pmatrix} \mathbf{H} \\ \tilde{\mathbf{H}} \\ \mathbf{h} \end{pmatrix}_{n+\frac{1}{2}} = \begin{pmatrix} \mathbf{H} \\ \tilde{\mathbf{H}} \\ \mathbf{h} \end{pmatrix}_{n-\frac{1}{2}} - \Delta t\mu^{-1}l\begin{pmatrix} \mathbf{S}_{\mathbf{H}} & 0 & 0 \\ 0 & \mathbf{S}_{\tilde{\mathbf{H}}} & 0 \\ 0 & 0 & \mathbf{S}_{\mathbf{h}} \end{pmatrix}^{-1}\begin{pmatrix} \mathbf{D}_{\mathbf{E}}^{(1)} & 0 & 0 \\ \mathbf{D}_{\mathbf{E}}^{(2)} & \mathbf{D}_{\tilde{\mathbf{E}}}\mathbf{Q} & 0 \\ 0 & \frac{1}{3}\mathbf{D}_{\tilde{\mathbf{e}}} & \frac{1}{3}\mathbf{D}_{\mathbf{e}} \end{pmatrix}\begin{pmatrix} \mathbf{E} \\ \tilde{\mathbf{e}} \\ \mathbf{e} \end{pmatrix}_{n} \\ \begin{pmatrix} \mathbf{E} \\ \tilde{\mathbf{e}} \\ \mathbf{e} \end{pmatrix}_{n+1} = \begin{pmatrix} \mathbf{E} \\ \tilde{\mathbf{e}} \\ \mathbf{e} \end{pmatrix}_{n} + \Delta t\varepsilon^{-1}l\begin{pmatrix} \mathbf{S}_{\mathbf{E}} & 0 & 0 \\ 0 & \mathbf{S}_{\tilde{\mathbf{e}}} & 0 \\ 0 & 0 & \mathbf{S}_{\mathbf{e}} \end{pmatrix}^{-1}\begin{pmatrix} \mathbf{D}_{\mathbf{H}} & \mathbf{D}_{\tilde{\mathbf{H}}} & 0 \\ 0 & \frac{1}{3}\mathbf{D}_{\tilde{\mathbf{h}}}\mathbf{P} & \frac{1}{3}\mathbf{D}_{\mathbf{h}}^{(2)} \\ 0 & 0 & \frac{1}{3}\mathbf{D}_{\mathbf{h}}^{(1)} \end{pmatrix}\begin{pmatrix} \mathbf{H} \\ \tilde{\mathbf{H}} \\ \mathbf{h} \end{pmatrix}_{n+\frac{1}{2}} \end{cases} \tag{A2}$$

Define $\mathbf{D_{intp}} = \mathbf{D_{\tilde{E}}}\mathbf{Q}$, and the two extended curl operator matrices can be rewritten as

$$
\bar{\mathbf{D}}_{\mathbf{E}} = \begin{pmatrix} \mathbf{D}_{\mathbf{H}}^{T} & 0 & 0 \\ \mathbf{D}_{\tilde{\mathbf{H}}}^{T} & \mathbf{D_{intp}} & 0 \\ 0 & \frac{1}{3}\mathbf{D_{\tilde{e}}} & \frac{1}{3}\mathbf{D_e} \end{pmatrix}
$$

$$
\bar{\mathbf{D}}_{\mathbf{H}} = \begin{pmatrix} \mathbf{D_H} & \mathbf{D_{\tilde{H}}} & 0 \\ 0 & 3\mathbf{D}_{intp}^{T} & \frac{1}{3}\mathbf{D}_{\tilde{e}}^{T} \\ 0 & 0 & \frac{1}{3}\mathbf{D}_{e}^{T} \end{pmatrix}. \quad (A5)
$$

The iterative formula for the e-field update has the form of

$$
\begin{pmatrix} \mathbf{E} \\ \tilde{\mathbf{e}} \\ \mathbf{e} \end{pmatrix}_{n+1} - \left(2\mathbf{I} - \frac{\Delta t^2 l^2}{\varepsilon\mu}\mathbf{B}\right)\begin{pmatrix} \mathbf{E} \\ \tilde{\mathbf{e}} \\ \mathbf{e} \end{pmatrix}_{n} + \begin{pmatrix} \mathbf{E} \\ \tilde{\mathbf{e}} \\ \mathbf{e} \end{pmatrix}_{n-1} = 0 \quad (A6)
$$

where

$$
\mathbf{B} = \begin{pmatrix} \mathbf{S_E} & 0 & 0 \\ 0 & \mathbf{S_{\tilde{e}}} & 0 \\ 0 & 0 & \mathbf{S_e} \end{pmatrix}^{-1} \begin{pmatrix} \mathbf{D_H} & \mathbf{D_{\tilde{H}}} & 0 \\ 0 & 3\mathbf{D}_{intp}^{T} & \frac{1}{3}\mathbf{D}_{\tilde{e}}^{T} \\ 0 & 0 & \frac{1}{3}\mathbf{D}_{e}^{T} \end{pmatrix}
$$
$$
\cdot \begin{pmatrix} \mathbf{S_H} & 0 & 0 \\ 0 & \mathbf{S_{\tilde{H}}} & 0 \\ 0 & 0 & \mathbf{S_h} \end{pmatrix}^{-1} \begin{pmatrix} \mathbf{D}_{\mathbf{H}}^{T} & 0 & 0 \\ \mathbf{D}_{\tilde{\mathbf{H}}}^{T} & \mathbf{D_{intp}} & 0 \\ 0 & \frac{1}{3}\mathbf{D_{\tilde{e}}} & \frac{1}{3}\mathbf{D_e} \end{pmatrix}.
$$

The matrix $\mathbf{B}$ can be rewritten as

$$
\mathbf{B} = \begin{pmatrix} \mathbf{S_E} & 0 & 0 \\ 0 & \mathbf{S_{\tilde{e}}} & 0 \\ 0 & 0 & \mathbf{S_e} \end{pmatrix}^{-1} \begin{pmatrix} \frac{1}{3}\mathbf{I_E} & 0 & 0 \\ 0 & \mathbf{I_{\tilde{e}}} & 0 \\ 0 & 0 & \mathbf{I_e} \end{pmatrix} (\mathbf{C_1} + \mathbf{C_2})
$$
$$(A7)$$

where

$$
\begin{aligned}
\mathbf{C_1} &= 3\begin{pmatrix} \mathbf{D_H}\mathbf{S_H^{-1}}\mathbf{D_H^T} + \mathbf{D_{\tilde{H}}}\mathbf{S_{\tilde{H}}^{-1}}\mathbf{D_{\tilde{H}}^T} & \mathbf{D_{\tilde{H}}}\mathbf{S_{\tilde{H}}^{-1}}\mathbf{D_{intp}} & 0 \\ \mathbf{D}_{intp}^{T}\mathbf{S_{\tilde{H}}^{-1}}\mathbf{D_{\tilde{H}}^T} & \mathbf{D}_{intp}^{T}\mathbf{S_{\tilde{H}}^{-1}}\mathbf{D_{intp}} & 0 \\ 0 & 0 & 0 \end{pmatrix} \\
&= 3\begin{pmatrix} \mathbf{D_H} & \mathbf{D_{\tilde{H}}} & 0 \\ 0 & \mathbf{D}_{intp}^{T} & 0 \\ 0 & 0 & 0 \end{pmatrix}\begin{pmatrix} \mathbf{S_H} & 0 & 0 \\ 0 & \mathbf{S_{\tilde{H}}} & 0 \\ 0 & 0 & \mathbf{S_h} \end{pmatrix}^{-1} \\
&\quad \cdot \begin{pmatrix} \mathbf{D_H^T} & 0 & 0 \\ \mathbf{D_{\tilde{H}}^T} & \mathbf{D_{intp}} & 0 \\ 0 & 0 & 0 \end{pmatrix} \quad (A8)
\end{aligned}
$$

and

$$
\begin{aligned}
\mathbf{C_2} &= \frac{1}{9}\begin{pmatrix} 0 & 0 & 0 \\ 0 & \mathbf{D_{\tilde{e}}^T}\mathbf{S_h^{-1}}\mathbf{D_{\tilde{e}}} & \mathbf{D_{\tilde{e}}^T}\mathbf{S_h^{-1}}\mathbf{D_e} \\ 0 & \mathbf{D_e^T}\mathbf{S_h^{-1}}\mathbf{D_{\tilde{e}}} & \mathbf{D_e^T}\mathbf{S_h^{-1}}\mathbf{D_e} \end{pmatrix} \\
&= \frac{1}{9}\begin{pmatrix} 0 & 0 & 0 \\ 0 & 0 & \mathbf{D_{\tilde{e}}^T} \\ 0 & 0 & \mathbf{D_e^T} \end{pmatrix}\begin{pmatrix} \mathbf{S_H} & 0 & 0 \\ 0 & \mathbf{S_{\tilde{H}}} & 0 \\ 0 & 0 & \mathbf{S_h} \end{pmatrix}^{-1} \\
&\quad \cdot \begin{pmatrix} 0 & 0 & 0 \\ 0 & 0 & 0 \\ 0 & \mathbf{D_{\tilde{e}}} & \mathbf{D_e} \end{pmatrix}. \quad (A9)
\end{aligned}
$$

Because the summation of two positive semi-definite matrices is still a positive semi-definite matrix, based on (A7), (A8), and (A9), the matrix $\mathbf{B}$ is a positive semi-definite matrix. Therefore, the field update process defined in (A1) is stable.

REFERENCES

[1] K. S. Yee, "Numerical solution of initial boundary value problems solving Maxwell's equations in isotropic media," *IEEE Trans. Antennas Propag.*, vol. 14, pp. 302–307, 1966.

[2] A. Taflove and S. Hagness, *Computational Electromagnetics: The Finite-Difference Time-Domain Method*, 3rd ed. Boston, MA: Artech House, 2005.

[3] K. S. Kunz and L. Simpson, "A technique for increasing the resolution of finite-difference solution of the Maxwell equation," *IEEE Trans. Elect. Compat.*, vol. 23, pp. 419–422, 1981.

[4] S. S. Zivanovic, K. S. Yee, and K. K. Mei, "A subgridding method for the time-domain finite difference method to solve Maxwell's equations," *IEEE Trans. Microw. Theory Tech.*, vol. 39, pp. 471–479, 1991.

[5] D. T. Prescott and N. V. Schuley, "A method for Incorporating different sized cells into the finite-difference time-domain analysis technique," *IEEE Microw. Guided Wave Lett.*, vol. 2, no. 11, pp. 434–436, 1992.

[6] M. J. White, M. F. Iskander, and Z. Huang, "Development of a multigrid FDTD code for three-dimensional applications," *IEEE Trans. Antennas Propag.*, vol. 45, no. 10, pp. 1512–1517, 1997.

[7] M. W. Chevalier, R. J. Luebbers, and V. P. Cable, "FDTD local grid with materials transverse," *IEEE Trans. Antennas Propag.*, vol. 45, pp. 411–421, 1997.

[8] M. Okoniewski, E. Okoniewska, and M. A. Stuchly, "Three-dimensional subgridding algorithm for FDTD," *IEEE Trans. Antennas Propag.*, vol. 45, no. 3, pp. 422–429, 1997.

[9] M. J. White, Z. Yun, and M. F. Iskander, "A new 3-D FDTD multigrid technique with dielectric traverse capabilities," *IEEE Trans. Microw. Theory Tech.*, vol. 49, pp. 422–430, 2001.

[10] P. Thoma and T. Weiland, "A consistent subgridding scheme for the finite difference time domain method," *Int. J. Numer. Modeling: Electron. Networks, Devices Fields*, vol. 9, pp. 359–374, 1996.

[11] O. Podebrad, "Finite Integration der Maxwellschen Gleichungen auf Lokal Verfeinerten Orthognalen Gittern," Ph.D. dissertation, Technical Univ. Darmstadt, Darmstadt, Germany, 2001.

[12] O. Podebrad, M. Clemens, and T. Weiland, "New flexible subgridding scheme for the Finite Integration Technique," *IEEE Trans. Magn.*, vol. 39, pp. 1662–1665, 2002.

[13] K. Krishnaiah and C. Raiton, "A stable subgridding algorithm and its application to eigenvalue problems," *IEEE Trans. Microw. Theory Tech.*, vol. 47, no. 5, pp. 620–628, May 1999.

[14] G. D. Smith, *Numerical Solution of Partial Differential Equations*. New York and London: Oxford Univ. Press, 1965.

[15] S. Wang and F. L. Teixeira, "Some remarks on the stability of time-domain electromagnetic simulations," *IEEE Trans. Antennas Propag.*, vol. 52, pp. 895–898, Mar. 2004.

[16] M. Marrone and R. Mittra, "A theoretical study of the stability criteria for hybridized FDTD algorithm for multiscale analysis," *IEEE Trans. Antennas Propag.*, vol. 52, no. 8, 2004.

[17] S. Wang, F. L. Teixeira, R. Lee, and J. Lee, "Optimization of subgridding scheme for FDTD," *IEEE Trans. Microw. Theory Tech.*, vol. 12, pp. 223–225, Jun. 2002.

[18] B. Donderici and F. L. Teixeira, "Improved FDTD subgridding algorithms vias digital filtering and domain overriding," *IEEE Trans. Antennas Propag.*, vol. 53, no. 9, pp. 2938–2951, 2005.

[19] K. Xiao, D. Pommerenke, and J. Drewniak, "A three dimensional FDTD subgridding algorithm based on interpolation of current density," in *Proc. IEEE EMC Symp.*, Santa Clara, CA, 2004, vol. 1, pp. 118–123.
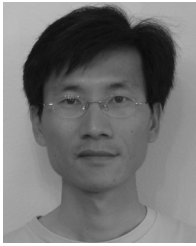
Kai Xiao (S'01–M'05) was born in Anshan, Liaoning province, China. He received the B.S. and M.S. degrees in electrical engineering from Tsinghua University, Beijing, China, in 1997 and 2000, respectively, and the Ph.D. degree from the University of Missouri at Rolla, in 2005.

He is currently a Senior Analog Engineer at Intel Corporation, DuPont, WA. His research interests include signal integrity, computational electromagnetics, and electromagnetic compatibility.

James L. Drewniak (S'85–M'90–SM'01–F'07) received the B.S., M.S., and Ph.D. degrees in electrical engineering from the University of Illinois, Urbana-Champaign, in 1985, 1987, and 1991, respectively.

He joined the Electrical Engineering Department, University of Missouri-Rolla, in 1991, where he is one of the principal faculty members in the Electromagnetic Compatibility Laboratory. His research and teaching interests include electromagnetic compatibility in high-speed digital and mixed-signal designs, electronic packaging, and electromagnetic compatibility in power electronic based systems.

David J. Pommerenke (SM'03) received the Ph.D. degree from the Technical University Berlin, Germany, in 1996.

After working at Hewlett Packard for five years he joined the Electromagnetic Compatibility Laboratory at the University of Missouri-Rolla in 2001 where he is a tenured Professor. His research interests include EMC, ESD measurement techniques and EMI analysis methods, numerical methods and instrumentation for EMC and high voltage. He has published more than 100 papers and is the inventor on seven patents. Besides other professional activities he is a U.S. representative of the ESD standard setting group within the IEC TC77b.